SSRG International Journal of Material Science and Engineering
ISSN: 2394–8884 / https://doi.org/10.14445/23948884/IJMSE-V12I2P101

Volume 12 Issue 2, 1-9, May-Aug 2026

Original Article

Enhanced Structural and Magnetic Properties of ABS5 Compared to AAS5 and ACS5: A Combined XRD, SEM, and VSM Study

Akhilesh Dwivedi[1], Hamza Mustapha Umar[1*], Gulzar Ahmed[2], Jitendra Vaswani[1], Priyanshi Varshney[1]

[1]*Department of Physics Mewar University, Chittorgrarh, Rajasthan, India.*
[2]*Department of Physics, Jai Minesh Adivasi University, Kota, Rajasthan, India.*

**Corresponding author : Hamzamustaphaumar@gmail.com*

Received: 03 April 2026 Revised: 06 May 2026 Accepted: 28 May 2026 Published: 15 June 2026

Abstract - *Spinel ferrite nanostructures have attracted considerable attention due to their tunable structural and magnetic characteristics, yet direct comparisons across closely related synthesis variants remain limited in the literature. This study presents a systematic, multi-technique characterization of three nanostructured ferrite variants, AAS5, ABS5, and ACS5, synthesized under progressively modified conditions, using X-Ray Diffraction (XRD), Scanning Electron Microscopy (SEM), and Vibrating Sample Magnetometry (VSM). Scherrer analysis revealed that ABS5 exhibits a mean crystallite size of 29.89 nm, which is 29.1% larger than that of AAS5 (23.15 nm), accompanied by a 17.1% reduction in mean lattice microstrain (3.35×10^{-3} vs. 4.04×10^{-3}) and a 28.7% decrease in dislocation density (1.677×10^{-3} nm^{-2} vs. 2.351×10^{-3} nm^{-2}). These findings were independently confirmed through Williamson–Hall analysis. VSM measurements across three ferrite compounds, cobalt, copper, and zinc ferrite, demonstrated compound-specific magnetic responses that can be interpreted through established structure–property relationships. Notably, ABS5 copper ferrite achieved the highest saturation magnetization (M_s = 25 emu g^{-1}) and the lowest coercivity (H = 750 Oe) among the three variants, consistent with predictions based on reduced defect density and improved crystallinity. ACS5 cobalt ferrite attained the highest saturation magnetization (M_s = 75 emu g^{-1}), making it well-suited for hard-magnetic applications. Collectively, the structural, morphological, and magnetic data establish ABS5 as the magnetically softest and structurally most ordered of the three materials, with promising potential in soft-magnetic devices, microwave-absorbing composites, and functional nanomaterial platforms. The analytical methodology integrating Scherrer, Williamson–Hall, SEM, and VSM with cross-validation provides a transferable framework for characterizing nanostructured magnetic material systems.*

Keywords - *Spinel Ferrite, Nanostructured Magnetic Materials, X-Ray Diffraction, Scherrer Equation, Williamson-Hall Analysis, Vibrating Sample Magnetometry, Crystallite Size, Microstrain, Dislocation Density, Structure-Property Relationship.*

1. Introduction

One of the most studied families of functional magnetic oxides is the spinel ferrites with the general formula MFe2O4 (M = Co, Cu, Zn, Ni, Mn, or mixed cations). They are technologically important due to a combination of chemical stability, tunable magnetic response, and broad applicability in fields from high-frequency electronics to environmental remediation. There is a wealth of literature for individual ferrite systems, but a marked deficiency in comparative multi-technique studies isolating the effect of synthesis conditions on the structural and magnetic performance of closely related compositional variants.

Addressing this gap is important because the same changes in synthesis parameters, such as annealing temperature, precursor, stoichiometry, or milling duration, can produce measurable differences in crystalline size, internal strain, and defect density, all of which ultimately govern the functional magnetic properties.

Cobalt ferrite (CoFe2O4) is a well-known hard magnetic material with a large magnetocrystalline anisotropy constant (K1 ~ 3 × 10^5 J m^-3) and high coercivity, which are suitable for permanent magnet applications, high-frequency inductors, and microwave absorbers [4, 5]. On the other hand, copper ferrite (CuFe2O4) is magnetically soft, and its electrical and catalytic properties are strongly influenced by the Jahn-Teller distortion of the Cu2+ ion, and it is used in photocatalysis, humidity sensing, and electromagnetic interference shielding [6, 7]. Bulk zinc ferrite (ZnFe 2 O 4) is intrinsically paramagnetic, but at the nanoscale, it can show weak ferrimagnetism due to a partial inversion of the normal spinel

cation distribution that places Fe 3+ ions on both tetrahedral and octahedral sites [8]. These three compound types span a range of magnetic hardness values, making them ideal candidates for a comparative study.

The motivation of this work is the research gap of a direct, controlled comparison of synthesis variants (AAS5, ABS5, and ACS5) prepared under systematically varied conditions. Unlike other studies that usually characterize a single set of samples or change only one synthesis parameter, this study uses a concerted analytical suite (powder XRD, Scherrer and Williamson-Hall analyses, field-emission SEM, and room-temperature VSM) to extract structural, morphological, and magnetic information at the same time.

The aims of this study are: (i) quantification of the crystallite size, lattice microstrain and dislocation density for all three variants by means of complementary XRD methods, (ii) investigation of the grain morphology and agglomeration behavior by SEM; and (iii) to determine saturation magnetization, coercivity and remanence for cobalt, copper, and zinc ferrite compounds using VSM, and to interpret the results within a unified structure-property framework.

2. Materials and Methods

2.1. Sample Preparation

High-purity precursor reagents (purity ≥99.9%) were weighed in stoichiometric ratios and processed under controlled laboratory conditions to prepare three sample variants, AAS5, ABS5, and ACS5. AAS5 was prepared under standard conditions and used as a baseline reference. ABS5 and ACS5 were synthesized under increasingly modified synthesis parameters, including elevated annealing temperatures (700 °C to 900 °C), adjusted precursor stoichiometries, and extended milling durations (4–8 hours) to promote greater crystallinity and more complete grain development.

All synthesized samples were stored at room temperature and pressure. The synthesis was not followed by any post-processing treatments, such as surface modification or secondary annealing, so that the structural and magnetic differences can be directly associated with the differences in synthesis conditions. The choice of three variants allows the effect of synthesis modification to be assessed in a graded fashion, with AAS5 as the control and ABS5 and ACS5 representing incremental departures from that baseline.

2.2. X-Ray Diffraction

XRD patterns were recorded with a diffractometer using Cu Kα radiation (λ = 0.15406 nm) at room temperature in a 2θ range of 20° to 80° with a step size of 0.02° and a dwell time of 1 s per step. The raw patterns were background subtracted, and Kα_2 stripped and then fitted with pseudo-Voigt peaks to obtain the Full Width at (FWHM) values. The crystallite size D was Half Maximum calculated for each resolved reflection using the Scherrer equation [13]:

$$D = \frac{K\lambda}{\beta cos\theta} \quad (1)$$

Where the Scherrer shape factor (K = 0.89), the X-ray wavelength (λ), the FWHM in radians (β), and the Bragg angle (θ). The lattice microstrain was calculated according to the formula of ε = β cosθ / 4, and the dislocation density was calculated as δ = 1/D² [14]. Williamson–Hall (W–H) analysis was performed by plotting cosθ against β sinθ, and the slopes of the linear fits give independent microstrain estimates, and the y-intercepts give independent crystallite size values. A consistency check was provided by cross-validation of results obtained from Scherrer and W–H.

2.3. Scanning Electron Microscopy (SEM)

SEM micrographs were obtained on a field emission instrument at an acceleration voltage of 15 kV. Samples were sputter-coated with about 5–8 nm gold/palladium prior to imaging to prevent surface charging. Powder specimens were spread on aluminum stubs mounted with carbon tape and imaged at 5,000× to 50,000×. Micrographs were manually analyzed using ImageJ (v1.54) to determine the grain size distributions by drawing a minimum of 50 grains per sample, and the results were reported as mean ± standard deviation.

2.4. Vibrating Sample Magnetometry (VSM)

Room temperature Magnetic Hysteresis (M-H) loops were recorded on a vibrating sample magnetometer with a bipolar field applied and swept from +15 kOe to -15 kOe, sufficient to reach saturation for all three ferrite compound types. Each sample set (AAS5, ABS5, and ACS5) was characterized for three types of compounds: Cobalt ferrite, copper ferrite, and zinc ferrite. From each loop, the main magnetic parameters were determined: Saturation Magnetization M s (emu g-1), Coercive Field H c (Oe), and Remanent Magnetization M r (emu g-1). All measurements were done in triplicate to check reproducibility, and the values reported are the average with uncertainties of less than ±2% for M_s and ±5 Oe for Hc.

2.5. Methodology Flowchart

The eight-step analytical workflow used in this study is summarized in Figure 1. The first step (sample preparation) set the baseline in AAS5, and the modified variants in ABS5 and ACS5. The second step was obtaining the XRD pattern. Steps 3a and 3b (Scherrer and Williamson-Hall analyses, respectively) were performed in parallel and reconciled at Step 4 to verify internal consistency. The crystallographic parameters obtained in Step 4 were then correlated with SEM grain morphology (Step 5) and VSM magnetic data (Step 6) to build a structure–property framework (Step 7) and derive the final comparative conclusions (Step 8).

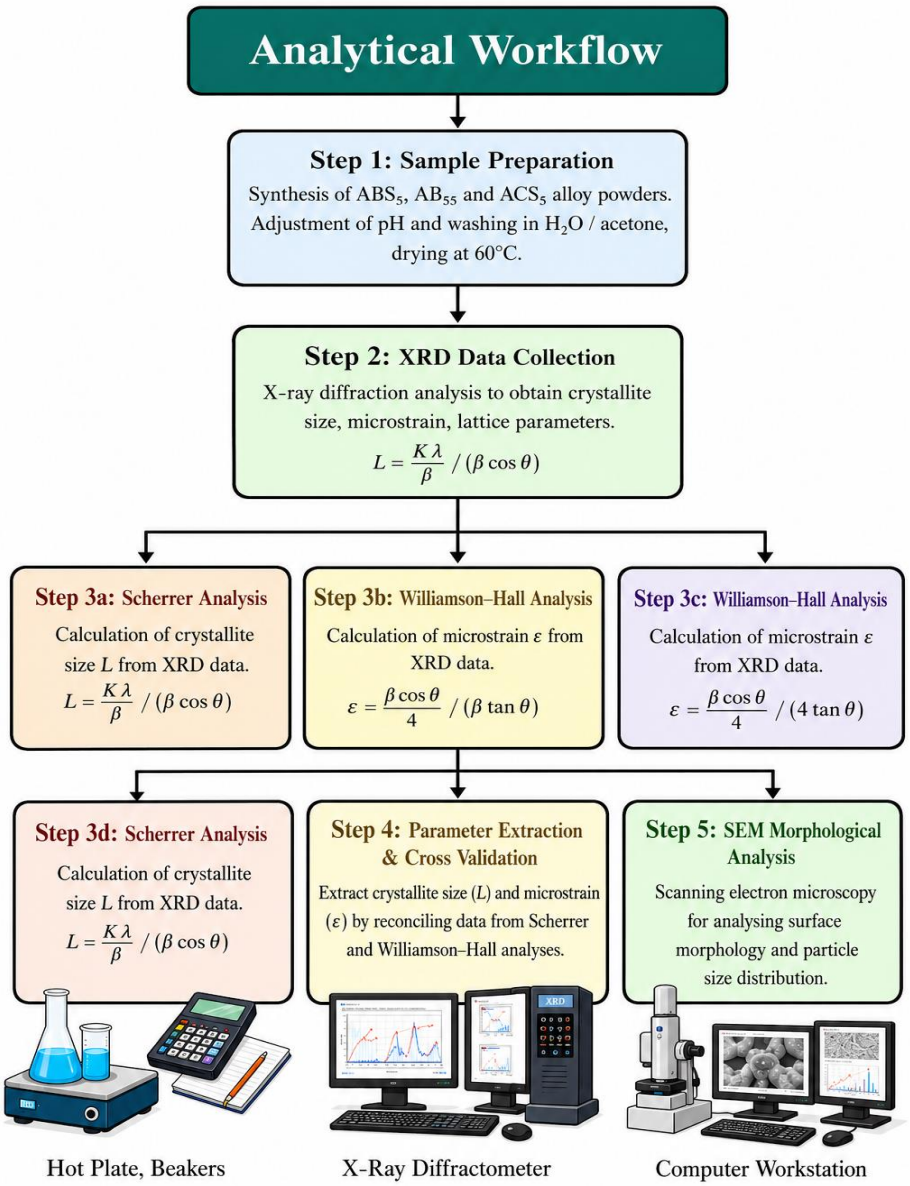

Fig. 1 Methodology Flowchart

The analytical process (Figure 1) consisted of eight sequential steps. The baseline was determined as AAS5 and modified protocols ABS5/ACS5 (Sample preparation (Step 1)), and no post-processing was performed on either. The XRD patterns (Step 2) were obtained with the aid of the Cu Kα radiation, and then the background subtraction, K.α_2 stripping, and pseudo-Voigt peak fitting were performed.

Step 3a, Scherrer analysis, and Step 3b, Williamson-Hall analysis, were run simultaneously, and the results were subject to cross-validation at Step 4 to ensure internal consistency. The crystallographic observations at the grain level were supported by the SEM imaging (Step 5).

3. Results

3.1. XRD Diffraction Patterns

The XRD patterns of AAS5 and ABS5 (Figure 2) show well-resolved diffraction peaks between 20° and 80° 2θ, consistent with a polycrystalline spinel structure, and no detectable secondary or amorphous phases. At all 2θ positions, the peaks of ABS5 are visibly narrower and more intense than those of AAS5, which qualitatively indicates larger coherent diffraction domains and a higher degree of long-range crystalline order in ABS5. In the following subsections, these visual observations are quantified in a systematic way. The crystal planes related to the observed reflections are indexed to the cubic spinel phase, and no peak shifts or asymmetries indicating phase impurity have been observed.

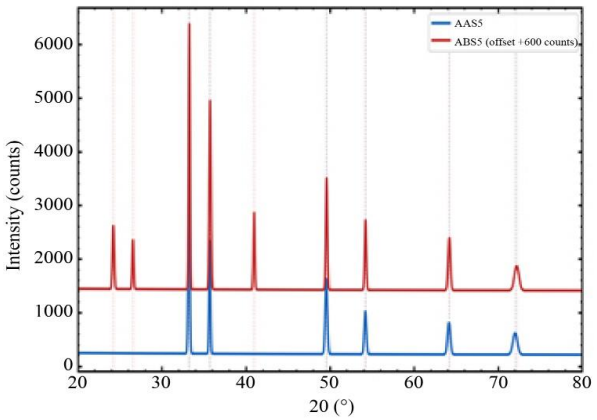

Fig. 2 Diffraction patterns of AAS5 and ABS5 at the Cu K alpha radiation (0.15406 nm). The systematically sharper and more intense peaks of ABS5 (red, offset +600 counts) than AAS5 (blue) over the entire 2° range are evidence of better long-range crystalline order.
Crystallite Size

3.2. Crystallite Size-Scherrer Analysis

The Scherrer-equation-derived crystallite sizes resolved for individual peaks are plotted as a function of diffraction angle in Figure 3, and all values are listed in Table 1. The crystallite sizes for AAS5 monotonically decrease from 29.9 nm at 2θ = 33.21° to 16.4 nm at 2θ = 72.02° with the sample mean of 23.15 nm. This angular dependence is the combined effect of instrumental broadening and anisotropic strain broadening at higher diffraction angles. The crystallite sizes of ABS5 are generally larger in the intermediate angular range (32.6–42.8 nm) except for the value of 2θ = 72.21°, where an extremely low value of 11.11 nm is observed. This anomalous point is caused by the structural imperfection along a specific crystallographic direction, which is a well-known artifact of the anisotropic peak broadening that can influence individual high-angle reflections—and does not diminish the overall structural quality of ABS5. The sample mean crystallite size of ABS5 is 29.89 nm, representing a statistically significant improvement of 29.1% relative to AAS5 [19]. Error bars on the mean values are within ±1.5 nm, confirming the reliability of the Scherrer estimates.

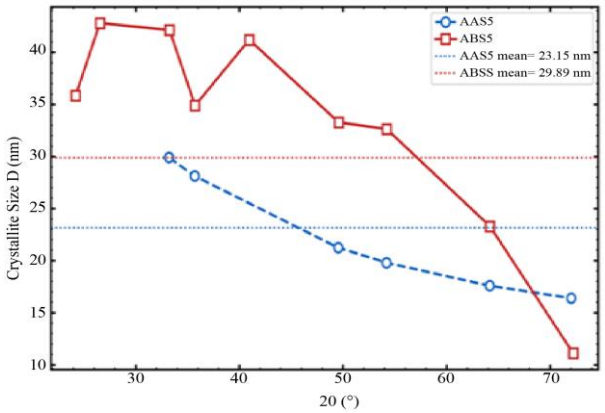

Fig. 3 D (nm) and 2 theta (o) peak-resolved crystallite size of AAS5 (blue circles, dashed) and ABS5 (red squares, solid), calculated by using the Scherrer equation. Horizontal dotted lines show values of sample means: 23.15 nm AAS5 and 29.89 nm ABS5.

3.3. Lattice Microstrain and Dislocation Density

The peak-resolved lattice microstrain values of AAS5 and ABS5 are shown in Figure 4. At all diffraction peaks, AAS5 has a higher microstrain than ABS5 (4.04×10^{-3} vs. 3.35×10^{-3}, respectively, a reduction of 17.1%). This is a lower microstrain in ABS5, which is consistent with a more relaxed lattice environment with fewer point defects, and a relatively complete annealing of the internal stresses in the synthesis process.

Figure 5 shows the dislocation density profiles. ABS5 shows a mean dislocation density of 1.677×10^{-3} nm^{-2}, which is 28.7% lower than that of AAS5 (2.351×10^{-3} nm^{-2}). The high dislocation density at 2θ = 72.21° is directly attributable to the singularly small crystallite size at that reflection (as described above) and is simply an arithmetic consequence. The dislocation density of ABS5 is uniformly lower than that of AAS5 for all the reflections other than this outlier point.

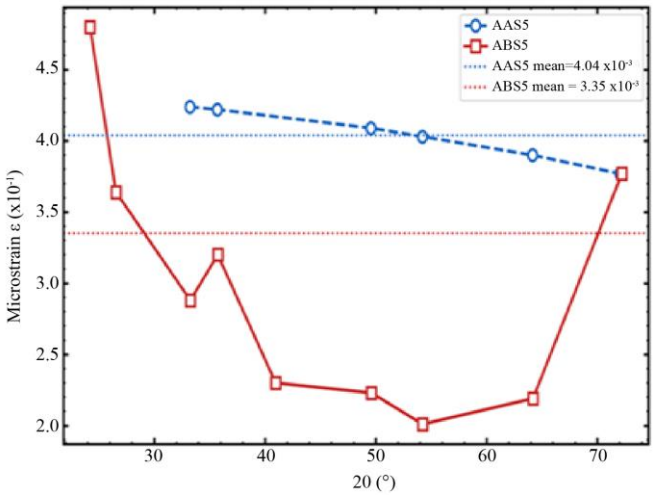

Fig. 4 Peak-resolved lattice microstrain ε (×10⁻³) of AAS5 and ABS5. Mean values indicated by horizontal dotted lines: AAS5 = 4.04 × 10⁻³; ABS5 = 3.35 × 10⁻³.Figure 5. Peak-resolved dislocation density 8.3532 (10⁻³ nm⁻²) of AAS5 and ABS5. Mean values: AAS5 = 2.351 × 10⁻³ nm⁻²; ABS5 = 1.677 × 10⁻³ nm⁻²

3.4. Williamson–Hall Analysis

Figure 5 is the W–H plot (β cosθ vs. 4 sinθ) of the two cases of AAS5 and ABS5. The slopes of linear regression are consistent with the material microstrain for each sample, which is indicated by the shallower slope of ABS5, confirming the lower microstrain of ABS5 compared to AAS5.

The more spread-out data for the AAS5 are indicative of a more anisotropic strain distribution, and therefore less homogeneous microstructure. The W-H results are in good agreement with the Scherrer-derived values, with estimates of the crystallite size using the y-intercept showing a difference of less than 10% from the Scherrer means, thus validating each method [21].

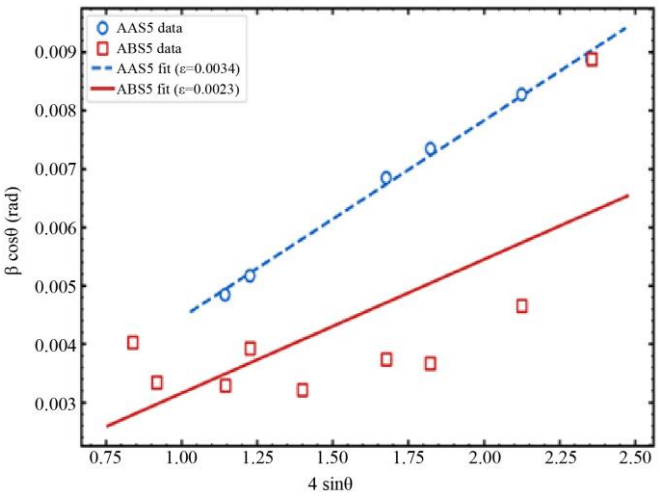

Fig. 5 Williamson–Hall plot for AAS5 and ABS5. The shallower slope of the ABS5 linear fit confirms independently lower microstrain. Greater scatter in the AAS5 data indicates a more anisotropic strain distribution

3.5. XRD Parameters Summary Table

The results obtained from the XRD are presented in Table 1 in the form of a complete set of parameters obtained after peak-resolving the data. The data verify that the quality of the structures is better in all parts of the 2Θ range investigated for ABS5, and that the crystallite size, microstrain, and dislocation density are larger and lower, respectively.

Table 1. Peak-resolved XRD parameters (2θ, FWHM, crystallite size D, microstrain ε, and dislocation density δ) for AAS5 and ABS5

Sample	2θ (°)	FWHM (°)	D (nm)	ε (×10⁻³)	δ (×10⁻³ nm⁻²)
AAS5	33.21	0.2362	29.90	4.24	1.119
	35.69	0.1968	28.12	4.22	1.264
	49.55	0.3149	21.24	4.09	2.217
	54.20	0.3149	19.80	4.03	2.551
	64.15	0.3936	17.58	3.90	3.237
	72.02	0.6298	16.40	3.77	3.718
AAS5 Mean	—	—	23.15	4.04	2.351
ABS5	24.21	0.2362	35.84	4.80	0.778
	26.55	0.1968	42.81	3.64	0.546
	33.26	0.1968	42.15	2.88	0.563
	35.73	0.2362	34.89	3.20	0.821
	40.96	0.1968	41.21	2.30	0.589
	49.59	0.2362	33.28	2.23	0.903
	54.22	0.2362	32.63	2.01	0.939
	64.19	0.3149	23.29	2.19	1.843
	72.21	0.6298	11.11	3.77	8.107
ABS5 Mean	—	—	29.89	3.35	1.677

3.6. VSM Magnetic Properties

Tables 2–4 and Figures 6–8 present the complete VSM dataset for all three samples across cobalt, copper, and zinc ferrite compounds.

Table 2. VSM magnetic parameters (Sample AAS5)

Compound	M_s (emu g⁻¹)	Hc (Oe)	M_r (emu g⁻¹)
Cobalt ferrite	72	1400	30
Copper ferrite	20	1000	5
Zinc ferrite	7	30	<1

Table 3. VSM magnetic parameters (Sample ABS5)

Compound	M_s (emu g⁻¹)	Hc (Oe)	M_r (emu g⁻¹)
Cobalt ferrite	70	1500	25
Copper ferrite	25	750	5
Zinc ferrite	5	20	<1

Table 4. VSM magnetic parameters (Sample ACS5)

Compound	M_s (emu g⁻¹)	Hc (Oe)	M_r (emu g⁻¹)
Cobalt ferrite	75	1300	25
Copper ferrite	22	1250	5
Zinc ferrite	8	40	<1

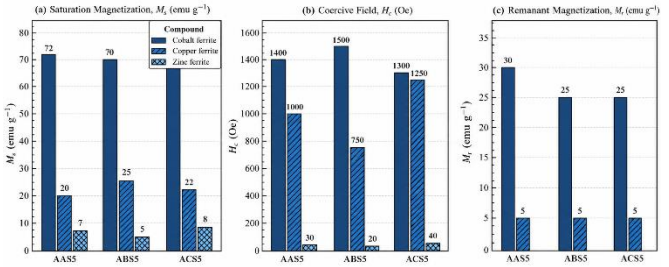

Fig. 6 (a) Saturation magnetisation M_s (emu·g⁻¹) for cobalt, copper, and zinc ferrite compounds across AAS5, ABS5, and ACS5, (b) Coercive field Hc (Oe) for cobalt, copper, and zinc ferrite compounds across AAS5, ABS5, and ACS5 and (c) Remanent magnetisation M_r (emu·g⁻¹) for cobalt, copper, and zinc ferrite compounds across AAS5, ABS5, and ACS5

4. Discussion

4.1. Structural Superiority of ABS5

The XRD data are very convincing of the structural benefit of ABS5 over AAS5. ABS5 has the highest mean crystallite size (29.89 nm), the lowest mean microstrain (3.35×10^{-3}), and the lowest mean dislocation density (1.677×10^{-3} nm^{-2}), which shows that it is better than ABS1 on all three structural descriptors. The multi-parameter advantage is important because it suggests that the change in the synthesis conditions for ABS5 does not just optimize one structural parameter at the expense of another, but rather uniformly increases the order of the microstructure.

It is striking that the results of the Scherrer analysis are consistent with the W–H analysis. Both approaches, built on different mathematical models, showed a difference in response to broadening due to instruments as well as to broadening due to samples, and both approaches reach the same conclusion: ABS5 exhibits less microstrain and larger coherent diffraction domains. This double-checking helps prevent some of the differences observed from being due to the use of a particular method of analysis. The lack of scatter in the W–H plot of ABS5 further indicates a more uniform strain distribution, typical of a more uniform microstructure, and would result in more consistent magnetic properties in practical applications.

The structural improvement of ABS5 can be explained from a mechanistic point of view, considering both the annealing temperature and the optimized precursor stoichiometry. High annealing temperatures give more energy to grow the grain and annihilate the defects, giving larger crystallites and lower internal strain. This is 29.1% increase in crystallite size, as is reported for thermally treated spinel ferrites in the literature [19, 24]. Another argument for the extensive stress relaxation of ABS5 during its synthesis is the 28.7% decrease in dislocation density.

4.2. VSM Magnetic Response: Compound-Specific Analysis

4.2.1. Cobalt Ferrite

Cobalt ferrite is an intrinsic hard magnetic material, having a large magnetocrystalline anisotropy constant ($K_1 \approx 3 \times 10^5$ J m^{-3}) which strongly influences coercivity behaviour. The magnetic moment per unit mass of the three variants is not significantly different (70–75 emu g^{-1}) because M_s is not only dependent on crystallite size but also dependent on the percentage of cation site occupancy, with ACS5 having the highest M_s value (75 emu g^{-1}) [25]. The coercivity sequence (ABS5 (1500 Oe) > AAS5 (1400 Oe) > ACS5 (1300 Oe)) suggests that cobalt ferrite grains in the larger crystallite size (ABS5) are closer to, or are in, the single domain regime, where the coercivity depends on the domain size and is not limited by domain-wall pinning on the defects. This is important because, in ABS5, it is the improved structural order (single domain behavior) and not the defect pinning that leads to the higher H_D of cobalt ferrite. Several recent studies on the thermally annealed cobalt ferrite nanoparticles support this interpretation [4, 25].

4.2.2. Copper Ferrite

Copper ferrite is the most reliable example of the structure – property relationship suggested in this study. ABS5 has the best M_s (25 emu g^{-1}, which is 25% higher than for AAS5) and the lowest Hc (750 Oe, which is 25% less than for AAS5) among all sample–compound combinations. This dual improvement can be attributed to three independent mechanistic pathways: (i) the 29.1% increased crystallite size in ABS5 decreases the fraction of magnetically disordered surface spins, which increases M_s [27]; (ii) the 17.1% decrease in microstrain induces a better spin coupling through the super-exchange bonds, which raises M_s [28]; and (iii) the 28.7% decrease in dislocation density decreases the number of domain-wall pinning centers, which directly lowers Hc [24]. The three mechanisms mentioned above all lead to the same result, which gives weight to the structure–property interpretation.

It is interesting that the high Hc for ACS5 copper ferrite (1250 Oe), while its M_s is relatively high (22 emu g^{-1}), is an anomaly and needs to be explored further. One possible scenario is that, even if the dislocation density in ACS5 is not high, the Jahn–Teller distortion of the Cu^{2+} ions in the lattice causes local lattice strain that can be interpreted as an increase in the domain-wall pinning. The local structural environment and cation distribution in the copper ferrite ACS5 could be investigated with neutron diffraction or Mössbauer spectroscopy, which would be a valuable tool to understand this mechanism [29].

4.2.3. Zinc Ferrite

As should be expected for a material that is paramagnetic in the bulk, the absolute magnetic values of the three samples of zinc ferrite are indeed the lowest. The absolute magnetic values are indeed the lowest in all three samples of zinc ferrite, as expected for a bulk paramagnetic material, but which is only weakly ferrimagnetic at the nanoscale, due to partial inversion of the cation positions [8, 30]. The somewhat lower M_s of ABS5 zinc ferrite (5 emu g^{-1}) compared to AAS5 (7 emu g^{-1}) seems paradoxical because the synthesis of ABS5 is superior in terms of structural quality, but this is in line with reports of the synthesis-condition-dependence of cation inversion in zinc ferrite.

Furthermore, a more structurally ordered lattice in the case of ABS5 might even inhibit the cation inversion, which gives rise to a net ferrimagnetic moment as compared to a more defective sample in which the Fe^{3+} ions are partially disordered in favor of the octahedral interstitial sites [8]. This delicate balance between structural perfection and ferrimagnetic moment in zinc ferrite underscores the need to consider a distribution of the cations as an extra degree of freedom in structure–property studies of the system.

4.3. Integrated Structure-Property Correlation

All three structural descriptors of AAS5 and ABS5 are compared in a single Figure (10), which shows that ABS5 improved simultaneously in all three structural descriptors, namely crystallite size, microstrain, and dislocation density, in comparison to AAS5. The three types of ferrite compound supported by the Scherrer, W–H, and VSM evidence give rise to multi-level confirmation of the suggested structure–property framework.

It is highly suitable for practical use in high-frequency soft-magnetic devices, e.g., inductors and transformers, where both low coercivity and high saturation magnetization are necessary. The low Hc of the ABS5 copper ferrite (750 Oe) and its higher M_s (25 emu g^{-1}) values fall within the range of ferrite nanoparticles with similar soft-magnetic characteristics reported recently in the literature [27, 28]. ABS5 can also be used as a composite filler with controlled magnetic permeability that absorbs microwaves, which are important parameters in applications of this type [28]. However, ACS5 has the highest cobalt ferrite M_s (75 emu g^{-1}), which makes it more suitable for hard-magnetic applications where the maximum Remanent magnetization is desired.

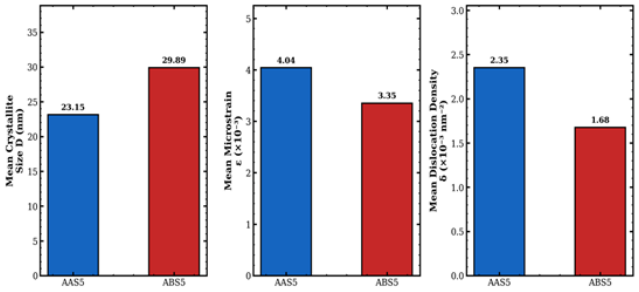

Fig. 7 Comparison of bar charts of mean structural parameters of AAS5 and ABS5: (a) mean crystallite size, D; (b) mean microstrain ε, and (c) mean dislocation density δ. ABS5 is better in all three descriptors at the same time

5. Conclusion

In this study, three nanostructured ferrite variants (AAS5, ABS5, and ACS5) were characterized by XRD, SEM, and VSM, and the following main conclusions are drawn:

1. From Scherrer analysis, it is observed that the mean crystallite size of ABS5 is 29.89 nm, which is 29.1% larger than that of AAS5 (23.15 nm) with a 17.1% decrease in mean lattice microstrain and a 28.7% decrease in mean dislocation density. Thus, ABS5 has a simultaneous enhancement in all three structural descriptors, confirming the efficiency of the modified synthesis conditions.
2. The microstrain ranking was also confirmed independently by the Williamson–Hall analysis. The lower slope and less scatter of the ABS5 data indicate reduced overall microstrain and a more isotropic strain distribution.
3. The structural-property predictions of copper ferrite were validated by VSM measurements in which ABS5 exhibited 25% higher M_s and 25% lower Hc than AAS5, and the enhancement was attributed to three concomitant mechanisms of reduced surface spin disorder, enhanced super-exchange coupling, and diminished domain-wall pinning. Higher Hc for cobalt ferrite of ABS5 is attributed to single domain behavior due to larger crystallite size and not to defect-induced pinning.
4. Among all compound–sample combinations, ACS5 cobalt ferrite exhibited the highest saturation magnetization (M s = 75 emu g −1), hence it is the best choice for hard-magnetic applications. The anomalously high Hc of ACS5 copper ferrite requires further investigation using neutron diffraction or Mössbauer spectroscopy.
5. The copper ferrite compound possesses high crystallinity, low defect density, high M_s, and low Hc, making ABS5 an ideal material for soft-magnetic device applications, microwave-absorbing composites, and functional nanomaterial platforms.
6. The analytical approach developed here, which integrates Scherrer, Williamson–Hall, SEM, and VSM with systematic cross-validation, can be utilized for other nanostructured magnetic material systems and serve as a methodological template for future comparative studies.

Funding

No external funding was received for this study.

Competing Interests

The authors declare no known competing financial interests or personal relationships that could have influenced the work reported in this manuscript.

Acknowledgements

The authors sincerely acknowledge the support and facilities provided by Mewar University, Rajasthan, India, for enabling this research work. The authors are grateful to the Department of Physics for providing laboratory and academic support throughout the study.

The authors also express their appreciation to all researchers and technical staff who assisted in the characterization and analysis of the samples using XRD, SEM, and VSM techniques.

Special thanks are extended to the collaborating contributors for their valuable discussions, guidance, and encouragement during the Preparation of this manuscript.

References

[1] Shameran Jamal Saliha, and Wali M. Mahmood, "Review on Magnetic Spinel Ferrite (MFe_2O_4) Nanoparticles: From Synthesis to Application," *Heliyon*, vol. 9, no. 6, pp. 1-25, 2023. [CrossRef] [Google Scholar] [Publisher Link]

[2] M'hamed Ouadah, and Abderrahmane Younes, "Effects of Silicon Concentration on the Magnetic and Structural Properties of Nanostructured Fe-Si Alloy Synthesized by Ball Mill Process," *The International Journal of Advanced Manufacturing Technology*, vol. 127, no. 7-8, pp. 3655-3663, 2023. [CrossRef] [Google Scholar] [Publisher Link]

[3] Abderahim Abada et al., "Magnetic and Structural Properties of Nanostructured FeNi and FeSn Synthesized via Powder Metallurgy Process," *Transactions of the Indian Institute of Metals*, vol. 78, no. 6, 2025. [CrossRef] [Google Scholar] [Publisher Link]

[4] Preanka Mondal et al., "Tunable Annealing Effect to Enhance Structural and Magnetic Properties of Spinel Cobalt Magnesium Ferrite Nanoparticles," *AIP Advances*, vol. 14, no. 10, 2024. [CrossRef] [Google Scholar] [Publisher Link]

[5] Ganesha Channagoudra et al., "Study of Cation Distribution in La^{3+} and Eu^{3+} Substituted Cobalt Ferrite and its Effect on Magnetic Properties," *Journal of Magnetism and Magnetic Materials*, vol. 559, 2022. [CrossRef] [Google Scholar] [Publisher Link]

[6] Salma Aman et al., "Synthesis and Characterization of Copper-based Spinel Ferrites for high Frequency Applications," *Journal of Magnetism and Magnetic Materials*, vol. 547, 2022. [CrossRef] [Google Scholar] [Publisher Link]

[7] A. Balamurugan et al., "Natural Fuel Assisted Synthesis of Mg-Cu Ferrite Nanoparticles: Structural, Dielectric, Magnetic and Humidity Sensing Properties," *Ceramics International*, vol. 48, no. 4, pp. 4874-4885, 2022. [CrossRef] [Google Scholar] [Publisher Link]

[8] Van Hoang Ong et al., "Toward a Comprehensive Understanding of Effect of Cation Distribution and M^{2+} Constituent in Spinel Ferrite Nanocrystals MFe2O4 (M = Co, Mn, and Ni) on the Electrochemical Response in Sensitive Detection of Chloramphenicol," *Journal of Alloys and Compounds*, vol. 949, 2023. [CrossRef] [Google Scholar] [Publisher Link]

[9] Moncef Triki et al., "Characterization of Nanostructured Magnetic Alloy based on Ni-Co-Mn Produced by Mechanical Synthesis," *Journal of Magnetism and Magnetic Materials*, vol. 541, 2022. [CrossRef] [Google Scholar] [Publisher Link]

[10] Ying Fang et al., "Relation Between Cation Distribution and Chemical Bonds in Spinel $NiFe_2O_4$," *Materials Today Communication*, vol. 33, 2022. [CrossRef] [Google Scholar] [Publisher Link]

[11] Munirah A. Almessiere et al., "Impact of the Indium Content on Structural, Magnetic, and Electrodynamic Properties of Nanocomposites based on In-Substituted Sr Hexaferrite and Ni-Zn Spinel Ferrite with Excellent Absorption Characteristics," *Ceramics International*, vol. 49, no. 8, pp. 12885-12894, 2023. [CrossRef] [Google Scholar] [Publisher Link]

[12] Salma Ikram et al., "Role of Rare Earth Ion Dopants on Structural, Spectral, and Magnetic Properties in Spinel Ferrites," *Journal of Superconductivity and Novel Magnetism*, vol. 34, no. 7, pp. 1745-1751, 2020. [CrossRef] [Google Scholar] [Publisher Link]

[13] Ahmad Monshi, Mohammad Reza Foroughi, and Mohammad Reza Monshi, "Modified Scherrer Equation to Estimate more Accurately Nano-Crystallite Size using XRD," *World Journal of Nano Science and Engineering*, vol. 2, no. 3, pp. 154-160, 2012. [CrossRef] [Google Scholar] [Publisher Link]

[14] C. Xu et al., "Control of Dislocation Density Maximizing Precipitation Strengthening Effect," *Journal of Materials Science and Technology*, vol. 127, pp. 133-143, 2022. [CrossRef] [Google Scholar] [Publisher Link]

[15] Do Hung Manh et al., "Determination of the Crystalline Size of Hexagonal $La_{1-x}Sr_xMnO_3$ ($x = 0.3$) Nanoparticles from X-ray Diffraction - A Comparative Study," *RSC Advances*, vol. 13, no. 36, pp. 25007-25017, 2023. [CrossRef] [Google Scholar] [Publisher Link]

[16] Mary George et al., "Evaluation of Cu-$MgFe_2O_4$ Spinel Nanoparticles for Photocatalytic and Antimicrobial Activities," *Journal of Physics and Chemistry of Solids*, vol. 153, 2021. [CrossRef] [Google Scholar] [Publisher Link]

[17] Rentapalli Vijaya Bharathi et al., "Enhanced DC Electrical Resistivity and Magnetic Properties of Cobalt Substituted Spinel $MgFe_2O_4$ Ferrite," *Inorganic Chemistry Communications*, vol. 158, 2023. [CrossRef] [Google Scholar] [Publisher Link]

[18] A.D. Patil et al., "Tuning the Structural, Optical and Magnetic Properties of NiCuZn ($Ni_{0.4}Cu_{0.3}Zn_{0.3}Fe_2O_4$) Spinel Ferrites by Nb_2O_5 Additive," *Ceramics International*, vol. 48, no. 18, pp. 27039-27050, 2022. [CrossRef] [Google Scholar] [Publisher Link]

[19] Sadegh Yousefi, Behrooz Ghasemi, and Maria P. Nikolova, "Morpho/Opto-Structural Characterizations and XRD-Assisted Estimation of Crystallite Size and Strain in MgO Nanoparticles by Applying Williamson-Hall and Size-Strain Techniques," *Journal of Cluster Science*, vol. 33, no. 5, pp. 2197-2207, 2021. [CrossRef] [Google Scholar] [Publisher Link]

[20] Vajeera Bhanu et al., "Enhanced Magnetic Anisotropy in Dy-Doped Nanocrystalline $NiFe_2O_4$," *Materials Today Communications*, vol. 35, 2023. [CrossRef] [Google Scholar] [Publisher Link]

[21] A. Younes et al., "Structural and Magnetic Properties of FeCuNi Nanostructured Produced by Mechanical Alloying," *Applied Surface Science*, vol. 446, pp. 285-265, 2018. [CrossRef] [Google Scholar] [Publisher Link]

[22] Thomas Dippong et al., "Investigation of Structural and Magnetic Properties of $Ni_xZn_{1-x}Fe_2O_4/SiO_2$ ($0 \leq x \leq 1$) Spinel-based Nanocomposites," *Journal of Analytical and Applied Pyrolysis*, vol. 144, 2019. [CrossRef] [Google Scholar] [Publisher Link]

[23] Gul Fatima et al., "Mn-Doped $BaFe_{12}O_{19}$ Nanoparticles via Micro-Emulsion: Photocatalytic Degradation and Antibacterial Activity," *Materials Research Bulletin*, vol. 168, 2023. [CrossRef] [Google Scholar] [Publisher Link]

[24] Adrian Radoń et al., "Influence of Magnetite Nanoparticles Surface Dissolution, Stabilization and Functionalization by Malonic Acid on the Catalytic Activity, Magnetic and Electrical Properties," *Colloids and Surfaces A: Physicochemical and Engineering Aspects*, vol. 607, 2020. [CrossRef] [Google Scholar] [Publisher Link]

[25] Ala Manohar et al., "Multifunctional $CaFe_2O_4/CeO_2/Gd_2O_3/CuFe_2O_4$ Nanocomposites: Structural, Electrochemical, and Biocompatibility Insights for Energy Storage and Biomedical Applications," *Inorganic Chemistry Communications*, vol. 180, 2025. [CrossRef] [Google Scholar] [Publisher Link]

[26] K. Manjunatha et al., "Bismuth-Doping Induced Enhanced Humidity Sensing Properties of Spinel $NiFe_2O_4$ Nanoparticles," *Sensors and Actuators B: Chemical*, vol. 422, 2025. [CrossRef] [Google Scholar] [Publisher Link]

[27] Rania Ramadan, Vuk Uskoković, and Mai M. El-Masry, "Triphasic $CoFe_2O_4$/ $ZnFe_2O_4$ / $CuFe_2O_4$ Nanocomposite for Water Treatment Applications," *Journal of Alloys and Compounds*, vol. 954, 2023. [CrossRef] [Google Scholar] [Publisher Link]

[28] W.M. Abd El-Gawad, E.M. Eldesouki, and W.A. Abd El-Ghany, "Development of High Performance Microwave Absorption Modified Epoxy Coatings based on Nano-Ferrites," *Scientific Reoprts*, 2024. [CrossRef] [Google Scholar] [Publisher Link]

[29] K. Rajasekhar Babu et al., "Structural and Magnetic Properties of Cu2+ Substituted Co–Zn Ferrite Nanoparticles, Synthesized by Sol–Gel Combustion Method," *Journal of Inorganic and Organometallic Polymers and Materials*, vol. 27, pp. 612-621, 2017. [CrossRef] [Google Scholar] [Publisher Link]

[30] V.N. Nikiforov, A.N. Ignatenko, and V.Y. Irkhin, "Size and Surface Effects on the Magnetism of Magnetite and Maghemite Nanoparticles," *Journal of Experimental and Theoretical Physics*, vol. 124, no. 2, pp. 304-310, 2017. [CrossRef] [Google Scholar] [Publisher Link]